Influence of Ellipsoidal Dimple Column Number on Performance of Highly-loaded Compressor Cascade

H. W. Lu[†], Y. P. Shi, J. C. Xin, X. Z. Kong and B. L. Peng

School of Naval Architecture and Ocean Engineering, Dalian Maritime University, Dalian, China

†*Corresponding Author Email: hwlu66@dlmu.edu.cn*

ABSTRACT

The impact of the column number of ellipsoidal dimples on a highly-loaded compressor cascade (NACA65-K48) under design conditions was investigated by using a numerical simulation method. Ellipsoidal dimples with a thickness of 0.2 mm were located at the position of chord length ranging from 10% to 36%. The span-wise interval was 5.0 mm. The performance and flow field structures of cascades with 1 to 5 ellipsoidal dimpled columns were compared, and the results showed that the turbulent kinetic energy intensity near the wall was enhanced and the fluid separation resistance was consequently improved. The total pressure loss was reduced by all modified ellipsoidal dimples. In addition, the separation bubble of the suction side was broken or weakened, the corner separation was improved, and the influence range of the passage vortex was reduced. Moreover, the improvement effect of cascade performance parameters initially increased with the increase in the number of dimple columns and then reduced as the number of columns was further increased. The reductions in the total pressure loss of the cascade were 0.59%, 1.47%, 1.69%, 1.91%, and 1.73% for column numbers 1 to 5, respectively.

1. INTRODUCTION

The utilization of highly-loaded stator blades are necessary because aeroengine structures are developing toward a high rotating speed and pressure ratio. However, with an increase in reverse pressure gradient, the separation of a boundary layer on a suction surface and the accumulation of low-energy fluid in a corner area become more evident, leading to increased flow losses, thus reducing the pressure-boosting capability of cascades (Liesner & Meyer, 2013). The key to solving this problem is to improve the separation resistance of low-energy fluids in grille channels. Recently, two control technologies have been commonly used: active (Liang et al., 2021) and passive (Xu et al., 2021) methods. Similar to winglets (Chen et al., 2019), dimples are used as a passive control. The momentum exchange between a low-energy fluid around a suction surface and the mainstream fluid is enhanced by a dimple, inducing the transition of the surface layer to occur earlier (Chung et al., 2021) and strengthening the separation-resistance ability of the cascade (Jeong & Song, 2021) by the dimple. In addition, the dimple structure can improve the heat transfer efficiency (Rao et al., 2015) and temperature distribution of the flow field (Amsha et al., 2017).

Dimples were first applied in the turbine cascades of gas turbines (Lake et al., 1999). In a low-pressure turbine

dimple depth study, Lan et al. (2011) concluded that dimples should be arranged such that the boundary layer thickness at the leading edge is less than the dimple depth. Rouser (2002) studied symmetric and non-stacked dimples in a Pak B turbine cascade and found that spherical dimples can reduce the total pressure loss by 28%. In addition, Casey et al. (2004), Sondergaard et al. (2004), and Chishty et al. (2011) concluded that dimples could reduce the total pressure losses in low-pressure turbines. They were applied to a low-speed compressor blade. Tian et al. (2015) illustrated that the compression ratio and differential pressure resistance increased by 9.8% and 19.24%, respectively, using dimple blades in low-speed centrifugal compressors. Zhao et al. (2016) studied two kinds of spherical dimples with a diameter of 1 mm and a depth-to-diameter ratio of 0.2 located at 30%–60% and 75%–95% of the axial chord length on the suction surface in a low-speed compressor. For the dimple blades under all angles of attack, the dimples arranged at 30%–60% of axial chord length were more effective to reduce total pressure losses than those located at 75%–95%.

In addition, other studies have shown that adding dimple structures to compressor blades can increase the pressure ratio and reduce the differential pressure resistance to a certain extent (Zinchenko et al., 2016). This is related to the depression of the separation by improving turbulent kinetic energy (D'Alessandro et al., 2019). Lu et al. (2019) explored the influence of spherical dimples

on the performance of high-speed and highly-loaded diffuser blades. They studied spherical dimples with different depths at a width-to-depth ratio of 0.25 and found that dimples of a specific size can eliminate the separation bubbles in the span direction of the blade and inhibit the separation in the corner area (Lu et al., 2018a). The influence of dimples arranged at different axial chord lengths on the performance of the blades was investigated, and the results showed that the total pressure loss of the dimples at 10%–32% of the axial chord length was the most reduced (Lu et al., 2018b). The results also illustrated that the parallel configuration of the spherical dimples had the most significant improvement on the performance of the cascade; however, the staggered arrangement of the dimples increased the total pressure loss (Wang et al., 2020). By studying the change in the dimple depth-to-print diameter ratio, it was found that the spherical dimples in the superior arc maintained the pressurization capacity and reduced the total pressure loss by 13.47% (Wang et al., 2022).

In summary, a more satisfactory performance was achieved using non-smooth surfaces in high-speed and highly loaded impellers. The influence of the location, size, and arrangement mode of the spherical dimples on the performance of a cascade was thoroughly investigated. Based on the abovementioned research, this study proposed axial long-axis ellipsoidal dimples that can be involved in more energy than spherical dimples. To compare the influence of dimples on cascade performance when different energies are involved, this study focused on a cascade with 1–5 rows of ellipsoidal dimples.

2. RESEARCH OBJECTS AND METHODS

2.1 Research Objects

The research object of this study was a high subsonic diffuser in-line blade NACA65-K48 (Zhang et al., 2015), a typical type of medium-pressure compressor or static mid-diameter blade (Fig. 1). Its specific parameters are listed in Table 1.

The prototype blade and ellipsoidal dimple blades with different column numbers were investigated in this study. All the ellipsoidal dimples were located at chord lengths ranging from 10% to 36% on the suction surface.

The spanwise spacing between two neighboring columns of the dimples was 5.0 mm. The depth (h) of the ellipsoidal dimple was 0.2 mm, the length of the semi-major axis (a) was 0.8 mm, and the length of the short semi-axis (b) was 0.5 mm, as shown in Fig. 2(a). The prototype blade described in the subsequent sections is represented by ORI for convenience. The blades with 1–5 columns of elliptical dimples are represented as Cases 1–5, respectively, as shown in Fig. 2(b).

2.2 Numerical Method Setting

The planar cascade investigated in this study had a certain symmetry. A half-blade passage and periodic boundary conditions on both sides of the flow passage were selected to reduce computational resources. To make the calculations more consistent with the experiments, the inlet boundary of the linear cascade model was 1.5c upstream from the leading edge. In contrast, the outlet boundary was 2c downstream from the trailing edge.
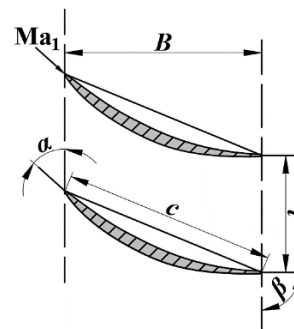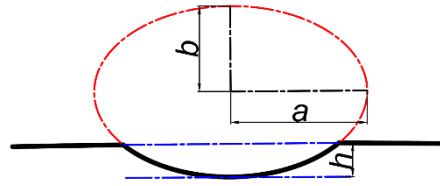

Fig. 1 Blade parameter

Table 1 Blade geometry and aerodynamic parameters

Parameters	Values	Units
Chord length c	60	mm
Axial chord B	55	mm
Blade pitch t	33	mm
Blade height H	100	mm
Inlet geometry angle α	48	°
Outlet geometry angle β	90	°
Inlet Mach number Ma_1	0.7	/
Reynolds number Re	694078	/

(a) Flow cross section of a dimple

Case 1   Case 2   Case 3

Case 4   Case 5
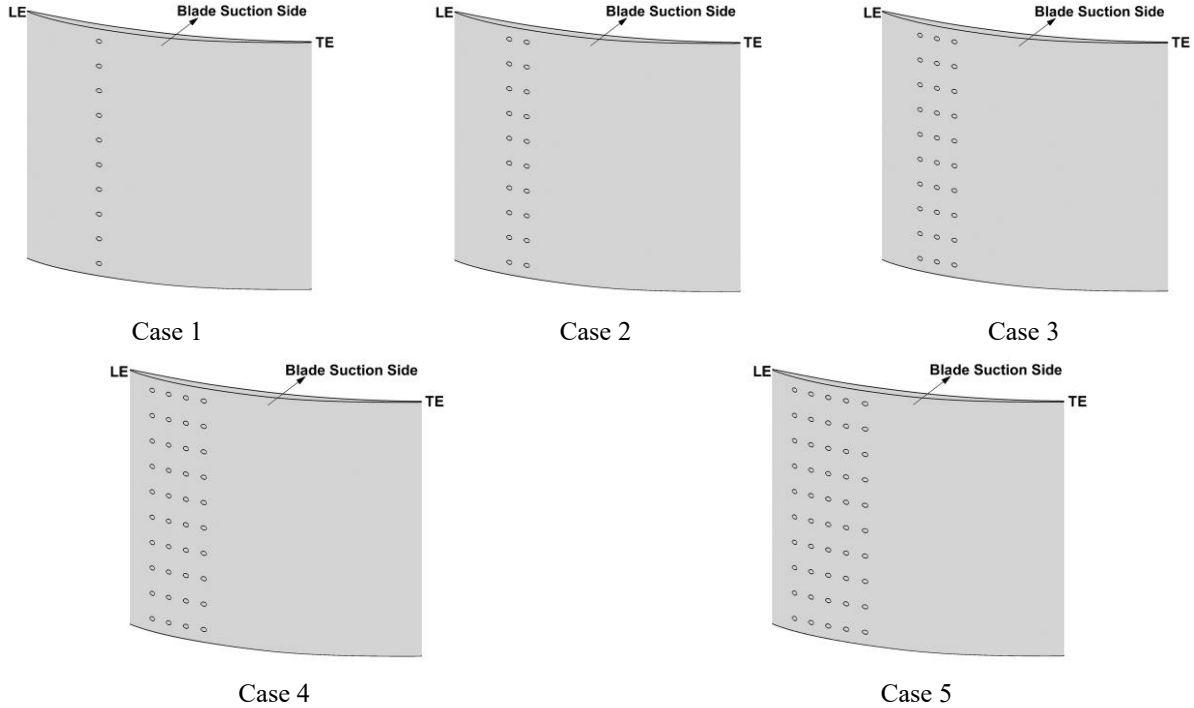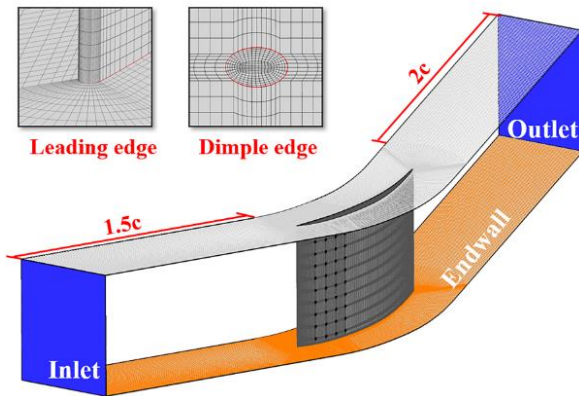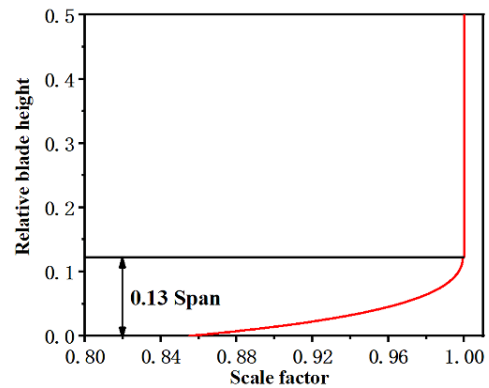
(b) Schematic of flow passage in different layout schemes

Fig. 2 Dimple structure and models of different layout schemes

(a) Grid division of the computing domain   (b) Total pressure coefficient at the inlet

Fig. 3 Grid division of the computing domain and total pressure coefficient at the inlet

Structured meshes were generated using the commercial grid-generation software ANSYS ICEM CFD, and the leading and trailing edges and the ellipsoidal dimples were encrypted locally. A structured mesh was installed inside the dimples, as shown in Fig. 3(a). Through the verification of grid independence (shown in Table 2) and the setting of calculation accuracy and time step, the total number of grids of the prototype cascade was approximately 1.7 million, and the grid number of a cascade with five columns of ellipsoidal dimples was approximately 9.8 million. When there were four columns of the ellipsoidal dimples, the grid number of the cascade was approximately 8.5 million. The ANSYS CFX software was used to solve this problem. The finite-volume method was applied to discretize and solve the compressible Reynolds time-average N-S equation.

The control equation group was closed by coupling the low Reynold number turbulent model (SST model) with the γ-θ transition model. Other boundary conditions, including the total pressure scaling factor (shown in Fig. 3(b)), temperature (310 K), turbulence (5%), and incident angle for the inlet, were determined based on the experimental conditions. The actual boundary layer distribution of the inlet was reflected by the total pressure
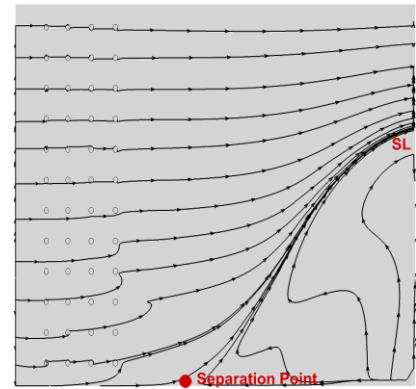
Table 2 Grid independence

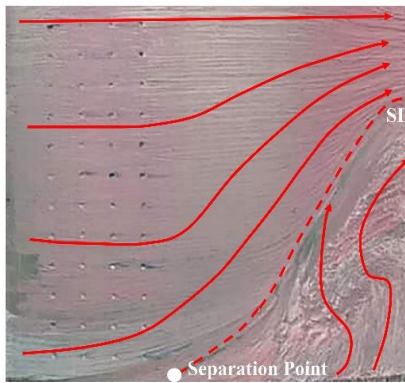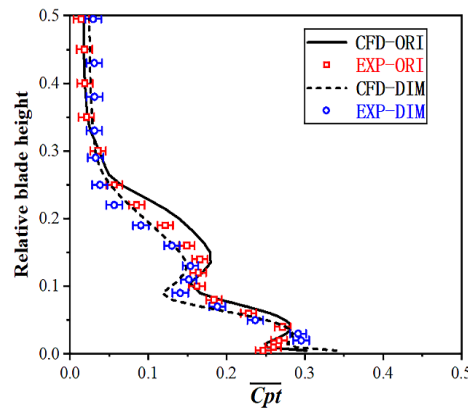| Models	Grid numbers	Outlet pressure/ *Pa*	Compre-ssion ratio
Proto-type model	599662	100874	1.209
	1695147	100185	1.177
	2081356	100180	1.177
Dimpled model	4798287	100752	1.189
	8495412	100829	1.184
	10846920	100842	1.184
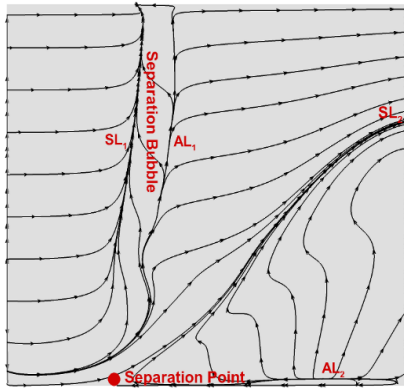
(a) CFD-ORI
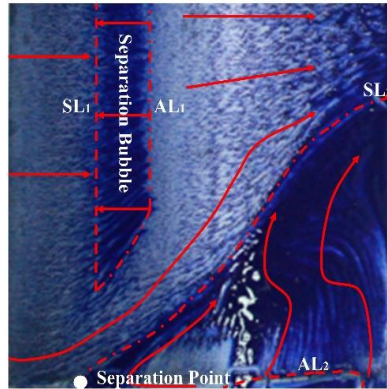
(b) EXP-ORI

(c)CFD- Dimple

(d)EXP- Dimple

(e) Pitch-averaged value of the total pressure loss coefficient

Fig. 4 Comparing the simulation results and experimental results

scaling factor. The average pressure at the outlet (101325 Pa) was also provided, and adiabatic and non-slip boundary conditions were applied to the blades and walls.

2.3 Validation of the Computational Method

The feasibility of the numerical simulation was verified by comparing the numerical and experimental results obtained in a high-speed linear cascade wind tunnel at Dalian Maritime University. First, the oil flowed at the suction surface, and limiting streamlines obtained through the simulation and experiment were compared, as illustrated in Figs. 4(a–d). The simulated and experimental total pressure loss coefficient distributions at the outlet are shown in Fig. 4(e). Figs. 4(a–d), clearly show good consistencies between the numerical limiting streamlines and experimental oil flow, particularly in the separation bubble, starting point, and radial separation range of the corner separation.

Second, the dimensionless total pressure loss coefficient of the cascade outlet was validated. In this study, 70% of the axial chord length downstream of the

trailing edge was at the outlet section, and the total pressure loss coefficient is defined as follows:

$$Cpt = (P_{t1} - P_{t2}) / (P_{t1} - P_1) \tag{1}$$

The error of the total pressure loss coefficient (ΔCpt) was approximately ±0.01. Moreover, the pitch-averaged value of the total pressure loss coefficient was:

$$\overline{Cpt} = \int Cpt dt \big/ t = \sum_{i=1}^{n}(Cpt_i \Delta t_i)\big/t \tag{2}$$

Figure 4(e) shows that the distribution trend and value of the coefficient along the blade height were consistent with the experimental results. Consequently, the flow phenomenon was accurately predicted using the selected computational model.

3. RESULTS AND DISCUSSION

To evaluate the impact of the ellipsoidal dimple column number on the performance of the cascade, the flow characteristics and vortex structure improvement in the cascade channel, and the performances of the ellipsoidal
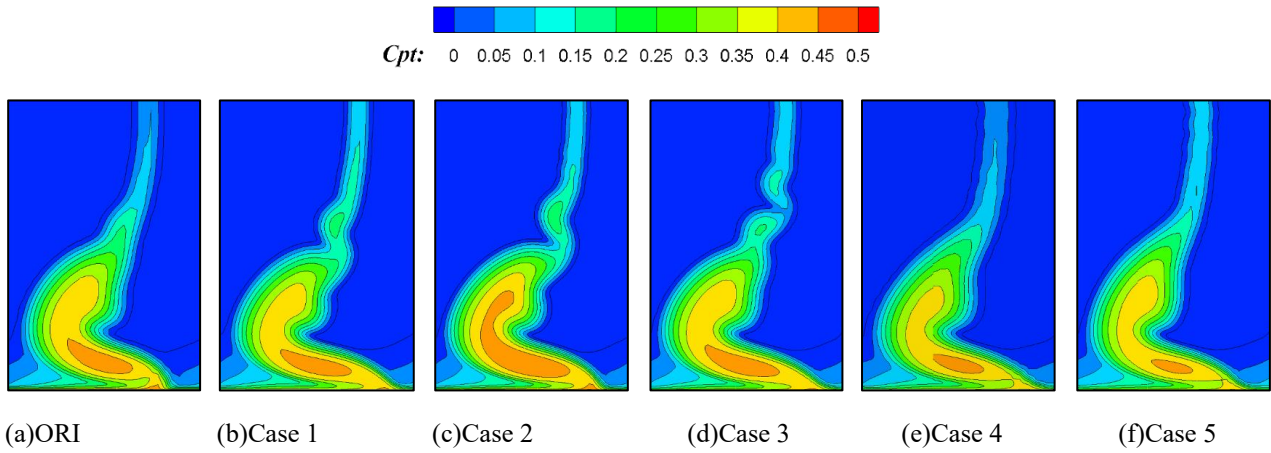
Cpt: 0 0.05 0.1 0.15 0.2 0.25 0.3 0.35 0.4 0.45 0.5

| (a)ORI | (b)Case 1 | (c)Case 2 | (d)Case 3 | (e)Case 4 | (f)Case 5 |

Fig. 5 Total pressure loss coefficient comparison at each cascade outlet section

dimpled cascades with different numbers of columns and the prototype cascade under the design conditions were compared.

3.1 Influence on Cascade Performance

The contours of the total pressure loss coefficients at the outlet section under the designed operating conditions are illustrated in Fig. 5. Blade-shaped losses were primarily concentrated in the corner area (Zhang et al., 2017). Compared to the prototype cascade, the total pressure coefficients of the ellipsoidal dimple cascade with different column numbers exhibited a significant difference in the corner area and wake. Moreover, Case 5 had an enormous impact on the corner area. The improvement effect of the ellipsoidal dimple cascade was optimal. However, the scale of the wake loss widened for all cascades with ellipsoidal dimples. In Cases 1–5, the influence scale of the wake gradually widened as the number of columns increased.

The variation of the total pressure loss coefficient induced by the ellipsoidal dimple column is illustrated in Fig. 6. When the number of ellipsoidal dimpled columns increased, the total pressure loss coefficient of the cascade first decreased and then increased. This phenomenon may be related to the increasing effect of ellipsoidal dimples on the flow mixing process as the column number increases. The increase in the total pressure loss coefficient in Case 5 was related to higher losses in the wake. To further reflect the performance improvement induced by the different dimpled cascades compared to the prototype cascade, the improvement fraction R_{crl} of the total pressure loss coefficient between the dimple cascade and prototype cascade is defined as

$$R_{crl} = (Cpt - Cpt_{ORI})/Cpt_{ORI} \times 100\% \qquad (3)$$

Compared with the prototype cascade, the total pressure losses in Cases 1–5 were reduced by 0.59%, 1.47%, 1.69%, 1.91%, and 1.73%, respectively.

To demonstrate the influence of the column number on the total pressure loss performance along the blade height, the distribution of the integrant-averaged total pressure loss coefficients for ORI, Case 2, and Case 4 along the relative blade height is shown in Fig. 7. The total pressure loss coefficient of the cascade with ellipsoidal dimples along a relative height of 0–0.08 was greater than that of the prototype cascade, which may be attributed to

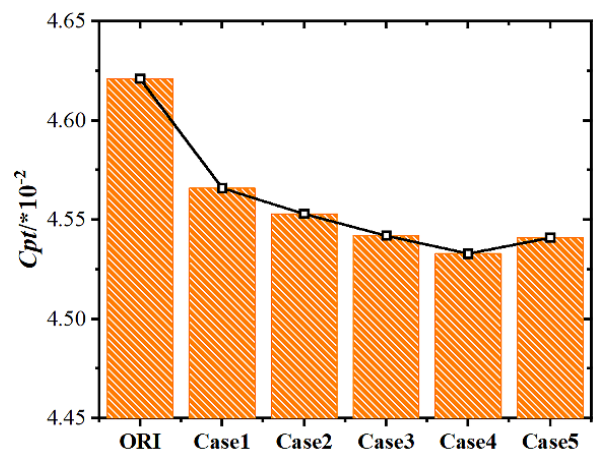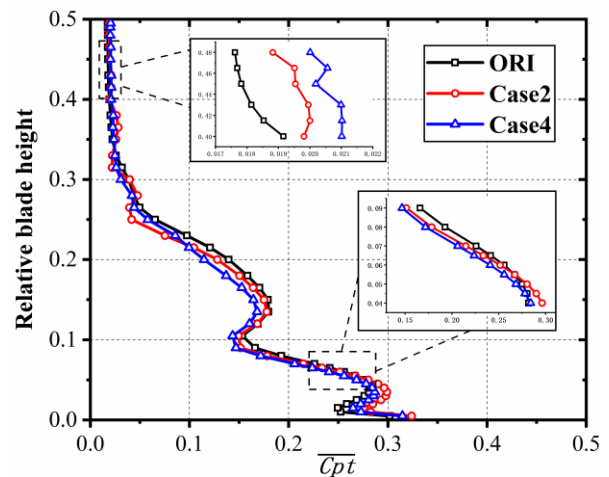**Fig. 6 Variation law of total pressure loss coefficient of each cascade**

Fig. 7 Distribution of integrant-averaged total pressure loss coefficient

the fact that a higher total pressure was lost owing to the convergence of the turbulent flow in the suction surface caused by dimples with the end wall boundary layer. Among the three cases, Case 4 introduced the smallest total pressure loss because it generated a significant
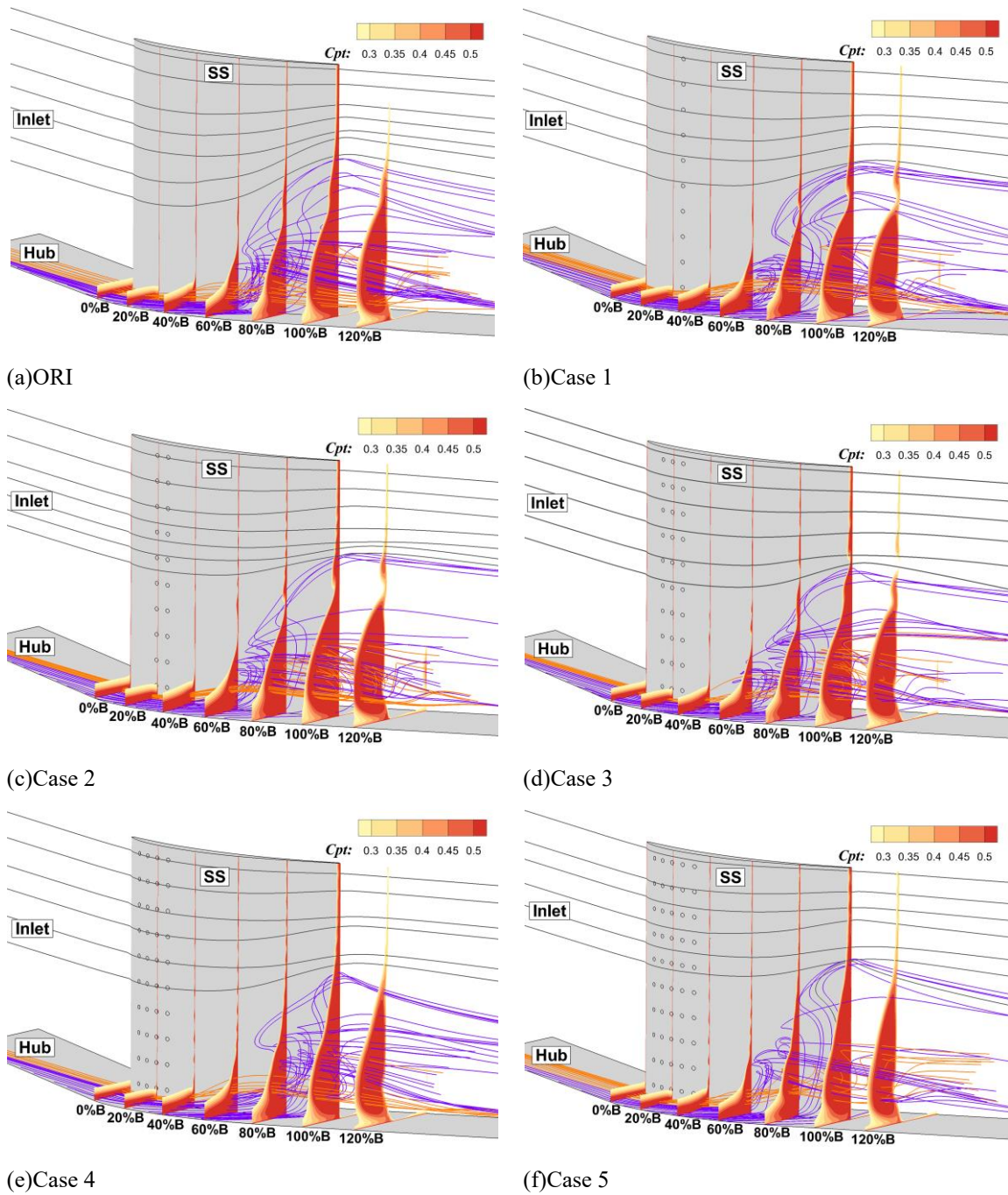
(a)ORI (b)Case 1

(c)Case 2 (d)Case 3

(e)Case 4 (f)Case 5

Fig. 8 Total pressure loss coefficient program for different axial sections and 3D streamline near the wall

turbulence that was not easily separated. The corner area was mainly distributed along a relative height of 0.08–0.32. The total pressure loss coefficient of the ellipsoidal dimpled cascades was smaller than that of the prototype cascade, and the optimum improvement effect was observed in Case 4. Along a relative height of 0.32–0.5, which was the wake area, the total pressure loss coefficient of the prototype cascade was the smallest, and those of Cases 2 and 4 increased, which could be caused by the thickness of the turbulent boundary layer and the three-dimensional flow effect (Cao et al., 2021).

The development of the total pressure loss coefficient along the axial direction and the three-dimensional streamline near the suction side and end wall areill ustrated in Fig. 8. The difference in the total pressure loss coefficient between the various ellipsoidal dimpled cascades was most significant at 120%*B*. The ranges of the corner area and high-loss core decreased to some extent for each modification. Compared with the prototype cascade, the separation vortex core in the corner area for Cases 1–5 gradually decreased. The phenomena in Cases 4 and 5 were the most obvious and were related to the difficulty of separation owing to the higher strength of the turbulence on the suction side. In addition, the flow capacity of the middle-diameter area of the cascade was higher, indicating that the reduction in static pressure was more significant at this point, resulting in low-energy fluid accumulation in the corner area along the span direction. This also explains the more significant wake loss in the dimpled cascade than in the prototype cascade, as shown in Fig. 7.

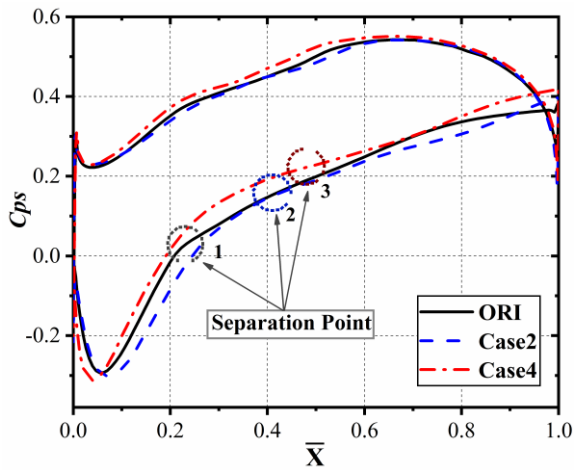To determine the variation in the blade loading

Fig. 9 Distribution curve of static pressure coefficient for blade surface at the end wall

capacity at the end wall of the blade, the distribution curves of the static pressure coefficients on the blade surface (Cps) for the prototype and Cases 2 and 4 cascades are shown in Fig. 9. The static pressure coefficient is defined as:

$$Cps = (P_{s2} - P_{s1})/(P_{t1} - P_{s1}) \qquad (4)$$

Numbers 1, 2, and 3 in the figure indicate the separation points at the suction surfaces of ORI, Case 2, and Case 4 cascades, respectively. The prototype cascade shows a slow increase in the static pressure coefficient after 25%c, whereas the turning points of Cases 2 and 4 increased to 42%c and 50%c, respectively, indicating a reduction in the corner area after adopting the ellipsoidal dimples. Moreover, an increase in the static pressure coefficients for both the suction and pressure sides was observed in Case 4. This was attributed to the improvement of the flow structure in the flow channel at the end wall induced by Case 4, which caused the entire flow channel to work under higher pressures.

3.2 Impact Mechanism for Ellipsoidal Dimple

The turbulent kinetic energy contour for the suction surface, static pressure coefficient contour for the end wall, and limiting flow lines for each border are illustrated in Fig. 10. A region with high turbulent energy existed at approximately 30%c in the prototype cascade. The downstream fluid migrated along the span direction, induced by fluid accumulation in the region with high turbulent energy, resulting in a separation bubble that caused significant flow losses. Compared with the prototype cascade, the fluid flowing through the suction surface of the cascade had a particular anti-separation ability induced by the ellipsoidal dimple in Case 1, such that the separation of the boundary layer moved backward. From the limiting streamline shown in Fig. 10, the separation bubble moved backward, and its range decreased. The height of the corner area decreased because the uplift of the corner area was further inhibited by the separation bubble. The separation bubble was not entirely broken by increasing the number of columns of the ellipsoidal dimples in Cases 2 and 3, which induced several separation lines to appear on the suction surface. However, the separation bubble was broken completely in

Cases 4 and 5, simplifying the flow structure of the cascades to be simpler. However, the suppression effect on the corner area induced in Cases 2–5 was weakened because of the breakage of the separation bubble.

The flow characteristics inside the ellipsoidal dimple are shown in Fig. 11 to illustrate the impact mechanism. A dimple near the mid-diameter of the blade in Case 4 was selected for this study. As shown in Fig. 11(a), the boundary layer was separated at the leading edge of the dimple (observed from the separation lines SL_1 and SL_2), and a set of recirculation zones inside the dimple was consequently generated. A closed structure that started at the saddle point (S_1) and ended at the node (N_1, N_2) was created by the separation. A set of separation spiral points (N_1 and N_2) formed inside the dimple, and the fluid departed from the interior of the dimple in the form of a separation vortex, which promoted mixing between the fluid inside the dimple and the surrounding fluid, as shown in Fig. 11(b). It should be noted that the reflow zone was asymmetric, which depended on the spanwise migration of the boundary layer.

The thickness developments of the boundary layers on the suction side of the prototype cascade and that at 45% of the blade height in Cases 2 and 4 are shown in Fig. 12. The results revealed that the boundary layer thickened because of the perturbation induced by the dimple. The thickness of the boundary layer of the prototype cascade was greater than that of the modified cascade at 30%c–40%c because separation bubbles appeared at this point in the prototype cascade, which is in agreement with the results shown in Fig. 10(a). The boundary layer in Case 4 transitioned earlier than that in Case 2 because the position of the first column of the ellipsoidal dimples in Case 4 was in front of that in Case 2. The boundary layer thickness of the modified cascade was greater than that of the prototype cascade after 60%c. The turbulent kinetic energy in Case 2 increased sharply at approximately 70%c, and the rate of increase of the thickness of the boundary layer in Case 2 became larger, as shown in Fig. 10(c).

3.3 Influence on cascade vortex structure

The characteristics of the passage vortex (PV) and the concentrated shedding vortex (CSV) on the suction surface can be reflected from cross-sectional streamlines. The cross-sectional streamlines at various axial locations inside the flow channel of the prototype cascade and that in Case 4 are shown in Fig. 13. The axial cross sections were located at 10%, 20%, 30%, 40%, 60%, 80%, and 100%B. The PV of the prototype cascade began to form at 30%B, whereas that in Case 4 was only observed at 40%B. The intensity and range of the PV in Case 4 were lower than those of the prototype cascade at 60% and 80%B. The corner region in Case 4 was slightly higher than that in ORI at 100%B, which is in agreement with the results shown in Figs. 8 and 10.

The vortex structures determined by the axial vorticity were analyzed to directly reflect the flow structure inside the flow channel of the cascade. The axial vorticity is defined as：

$$W_x = \partial V_z / \partial y - \partial V_y / \partial z \qquad (5)$$

The velocity that indicates a counterclockwise rotation when viewed from the outlet direction is positive, and that indicates clockwise rotation is negative.

(a)ORI

(b)Case 1

(c)Case 2

(d)Case 3

(e)Case 4

(f)Case 5
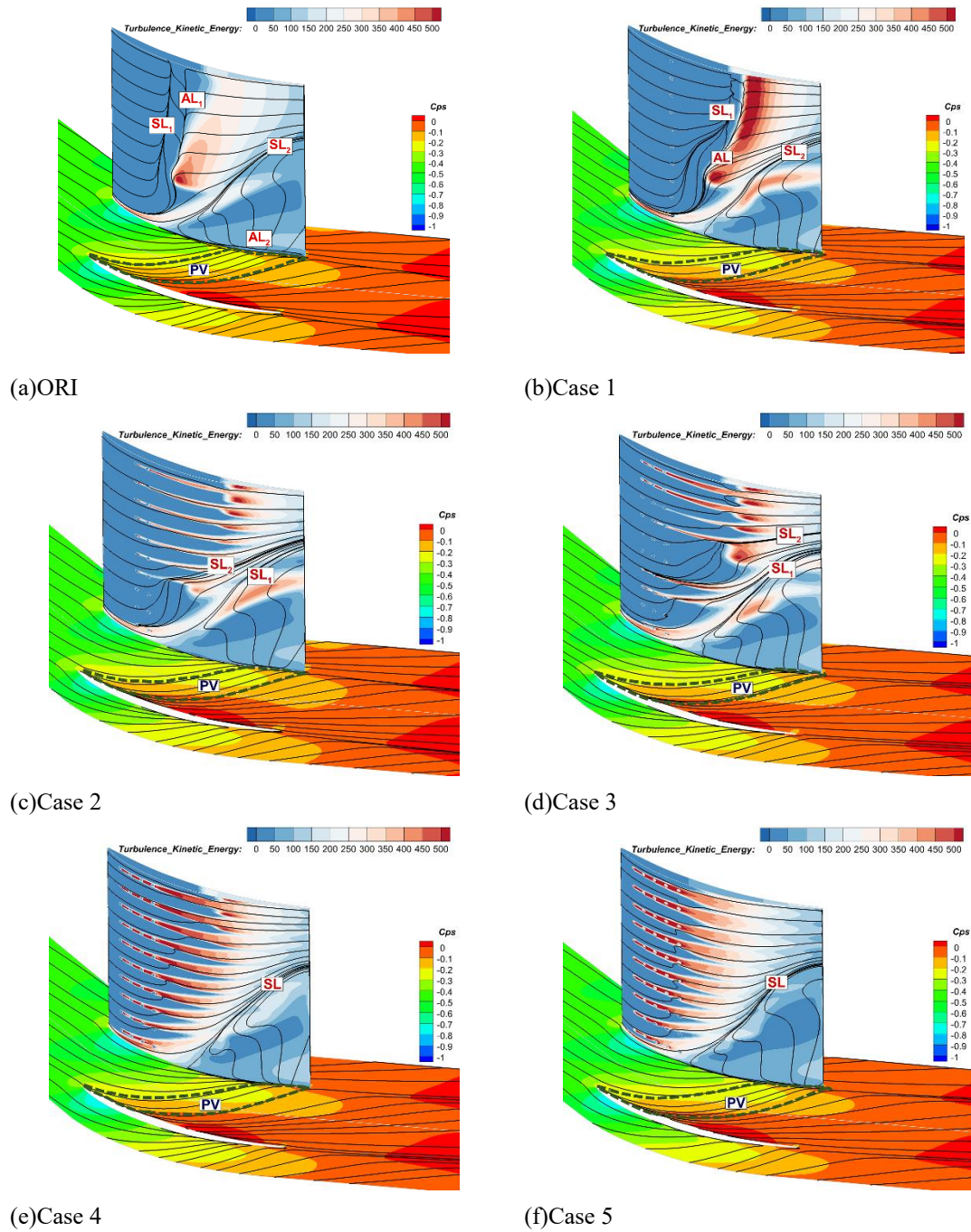
Fig. 10 Turbulent kinetic energy on suction surface, *Cps* on end wall, and limiting streamline near the wall

(a) Limiting streamline in dimple

(b) Streamline in the middle section of dimple
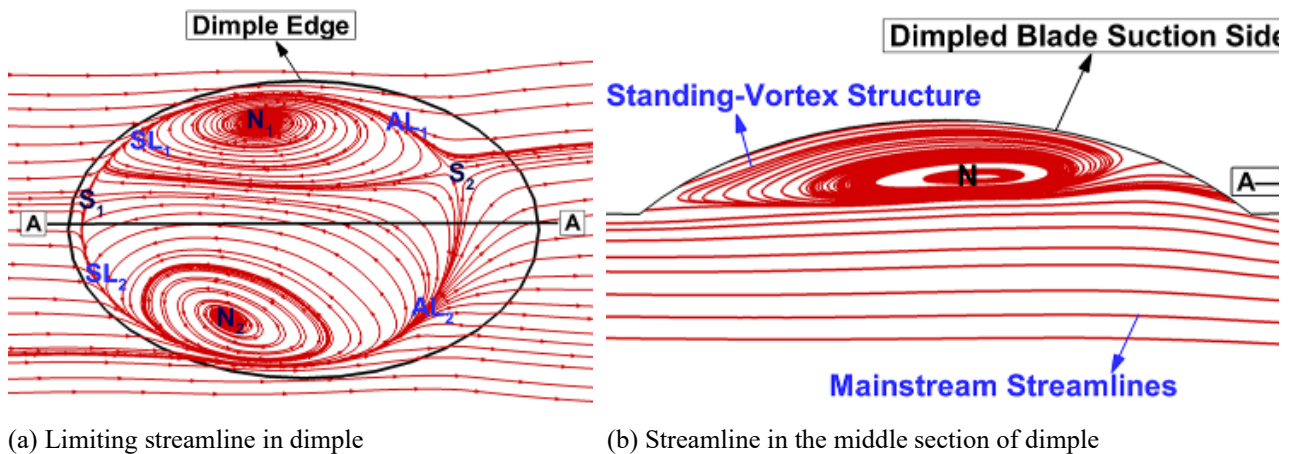
Fig. 11 Flow characteristics in dimples
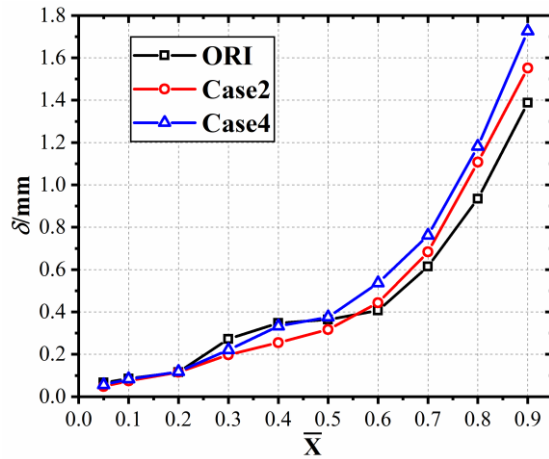
Fig. 12 Thickness development of the boundary layer

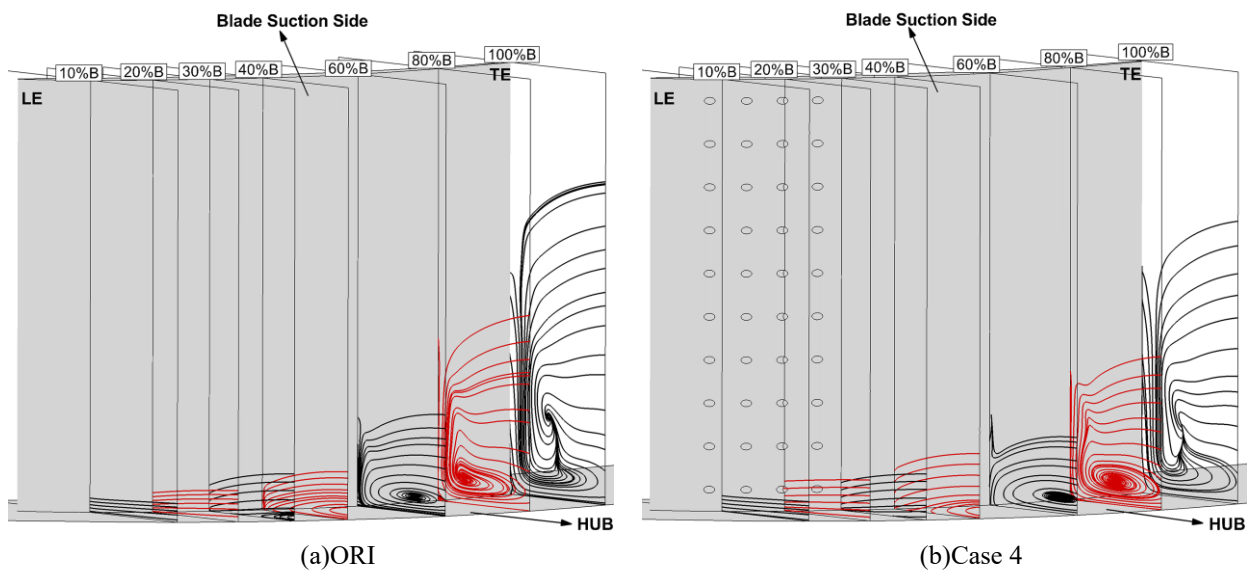(a)ORI   (b)Case 4
Fig. 13 Streamlines in the different sections in ORI and Case 4 cascades

The distributions of the axial vorticities of all the cascades used in this study are shown in Fig. 14, where the axial cross-sectional position is the same as that shown in Fig. 8. It can be observed that there were several areas of high vortex concentration in the cascade channel. Based on the results of the vortex structure in the diffuser cascades (Chen et al., 2017), these high-vortex areas included those of the pressure-side horseshoe vortex (HVP), suction-side horseshoe vortex (HVS), end wall spreading vortex (SV), passage vortex (PV), wall vortex (WV), concentrated shedding vortex (CSV), trailing edge shedding vortex (TSV), and trailing edge wall corner vortex (CV). In the prototype cascade, as the airflow flowed axially, the boundary layer thickness on the end wall gradually increased, and the source of the axial vorticity was generated close to the wall. By combining the limiting streamlines of the end wall shown in Fig. 10(a), it is clear that the low-energy fluid mass in the boundary layer of the end wall was driven to the suction surface and began to accumulate near the 40%*B* position owing to the transverse pressure gradient. In contrast, the low-energy fluid mass migrated along the span direction, and the SV began to form. From this position to the trailing edge of the cascade, the influencing range and intensity of

the PV system developed by the HVP gradually expanded and strengthened. Near 80%*B*, a WV with negative vortices was generated owing to the effect of the PV on the low-energy fluid in the surrounding boundary layer. In addition, a CV was formed owing to the 'rubbing' effect of the transverse and spanwise secondary flows. The intensity of the PV peaked at the trailing edge of the cascade. In addition, the CSV developed by the WV entered the flow-path region at the trailing edge. A TSV was created by combining the suction surface boundary layer, end wall boundary layer, and part of the PV, owing to the influence of the CSV and PV. The intensity of the PV gradually decreased as the transverse pressure gradient was no longer present, and was stable in the flow field when the CSV, TSV, and CV were at 120%*B*.

The results shown in Fig. 14 also demonstrate that the intensity of the WV was strengthened by every column of the ellipsoidal dimple cascade compared with the prototype cascade. The PV was formed after 60%B, and the strength and range of the PV caused by the ellipsoidal dimple cascade were reduced by integrating, as shown in Fig. 10. The starting position of the CV induced by the PV shifted back and its strength was weakened. The CV disappeared in Cases 3, 4, and 5 at 120%B. The intensity
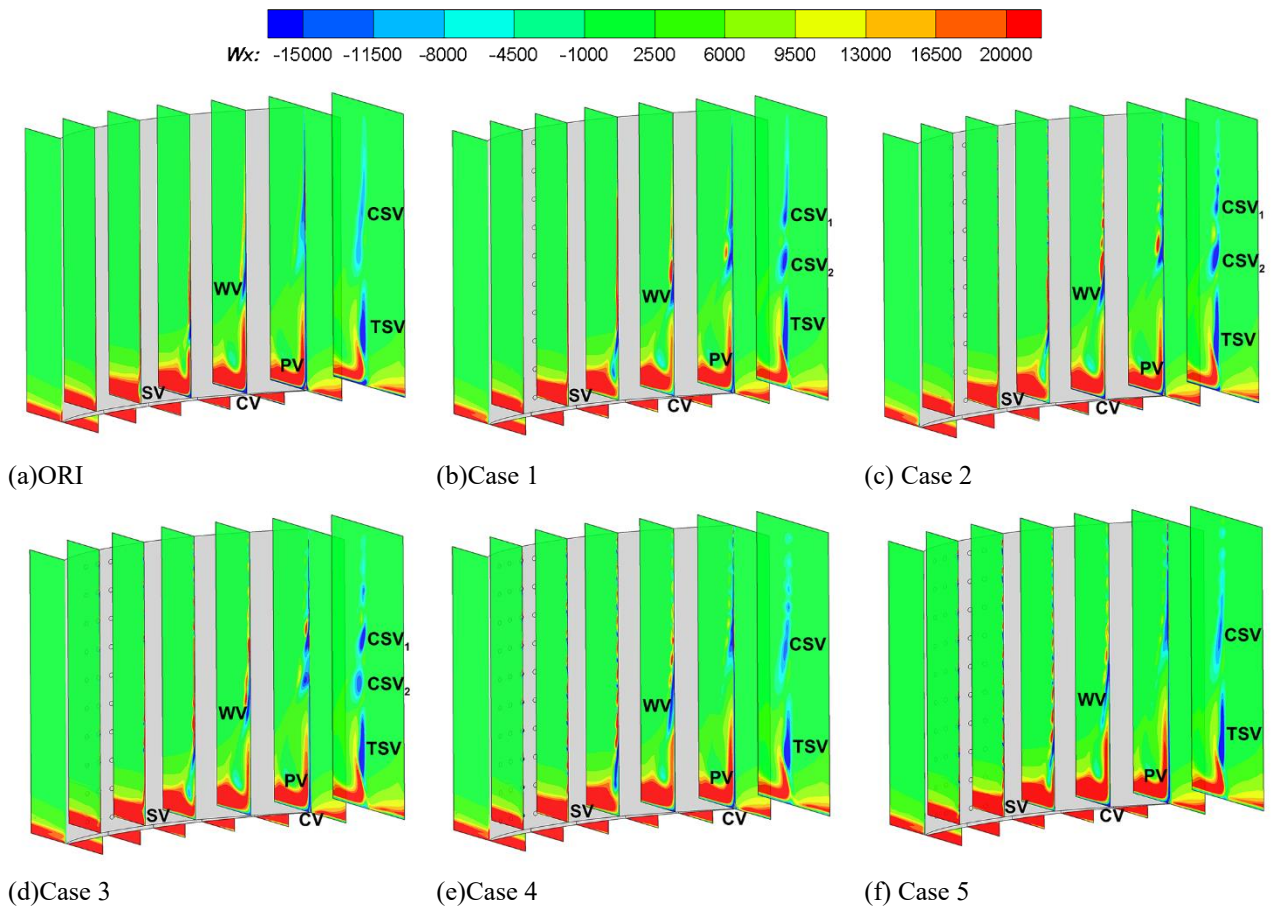
(a)ORI   (b)Case 1   (c) Case 2

(d)Case 3   (e)Case 4   (f) Case 5

Fig. 14 Axial vorticity distribution

(a)ORI   (b)Case 1   (c)Case 2

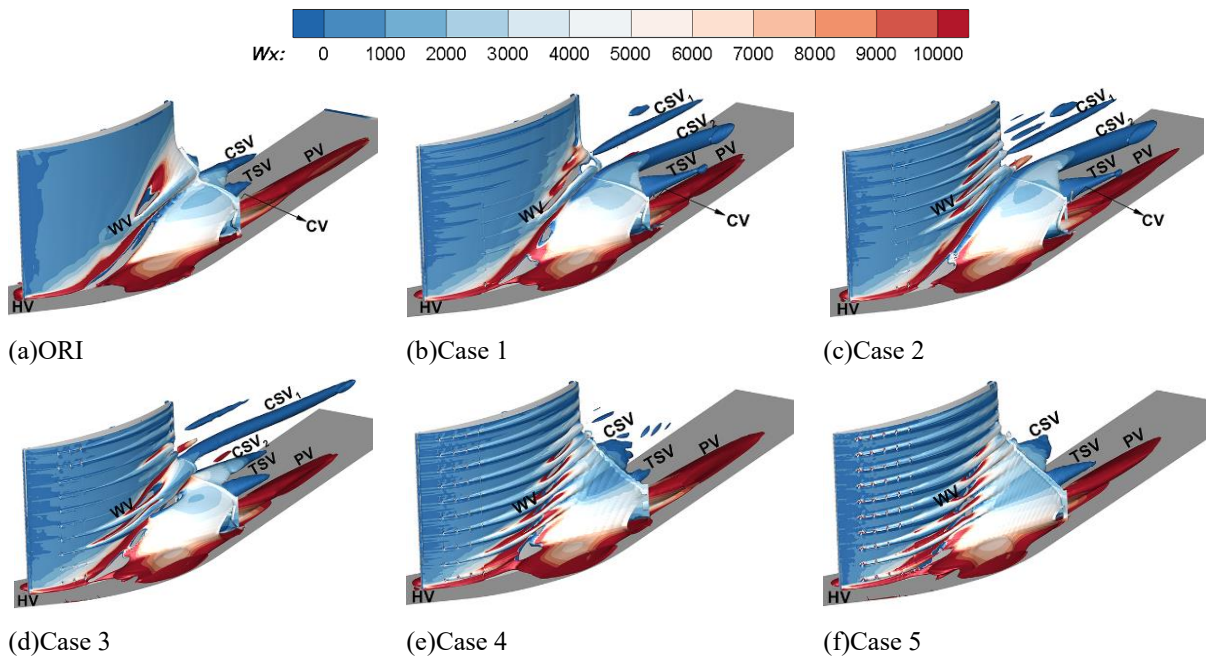(d)Case 3   (e)Case 4   (f)Case 5

Fig. 15 *Q*-Criterion iso-surface rendered by axial vorticity

of the CSV induced by the modified cascades was weakened. Moreover, several apparent CSVs were generated in Cases 1, 2, and 3 because the separation bubbles were not completely broken. In addition, the improvement in CSV in Cases 4 and 5 was the most significant. However, compared to Case 5, Case 4 had a smaller TSV range.

The distinction between distributed and concentrated vortices using axial vortices is not apparent and has some limitations. Therefore, a three-dimensional vortex structure and cross-sectional streamlines were drawn as a supplement based on the vortex determination *Q* criterion.
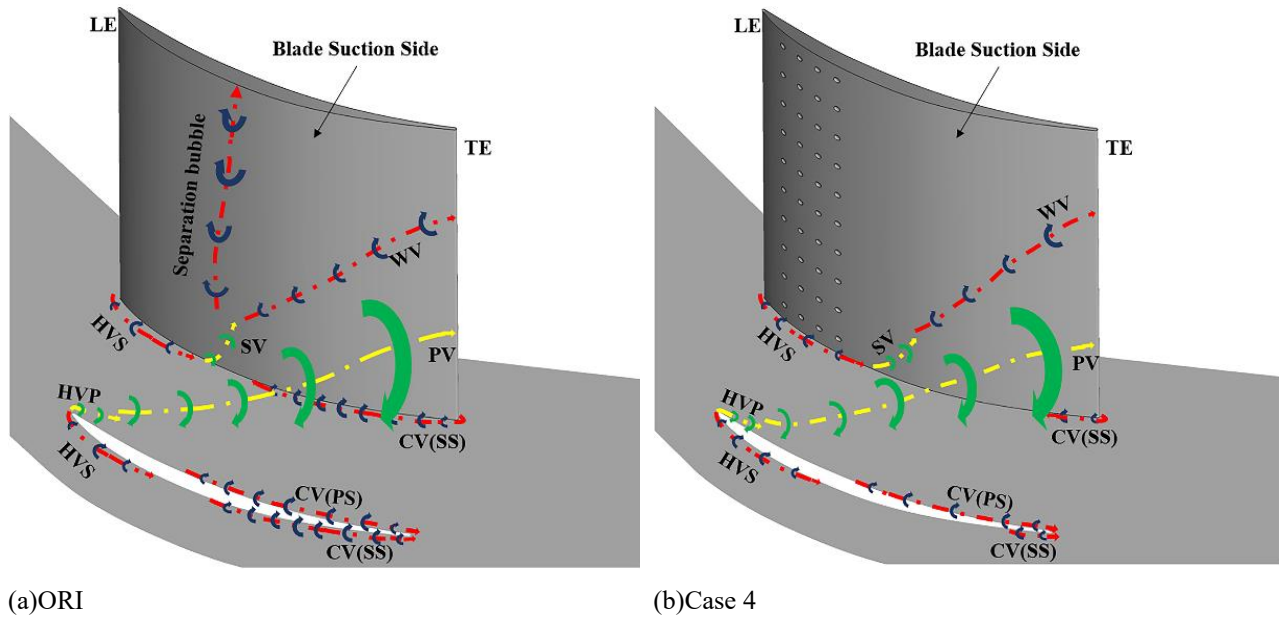
(a)ORI

(b)Case 4

Fig. 16 Three-dimensional vortex structures in ORI and Case 4

Q is defined as：

$$Q = 1/2\left(\Omega_{ij}\Omega_{ij} - Si_jSi_j\right) \tag{6}$$

The effect of the ellipsoidal dimple on the flow field of the cascade was more directly reflected by the three-dimensional vortex structure identified by the Q criterion. The three-dimensional vortex structure of the flow field caused by the axial vorticity is shown in Fig. 15, and an iso-surface $Q = 10^7$ was considered in this study. The low-energy fluid accumulated in the prototype cascade owing to the separation of the corner area significantly influenced the flow capacity of the cascade. The intensity of the vortices associated with the corner area was substantially weakened by the four-column ellipsoidal dimples in Case 4. The ranges of the corner area, CSV, and TSV also decreased considerably.

The main vortex structures in one flow channel of the prototype and Case 4 cascade are shown in Fig. 16. In the abovementioned figure, CV (PS) and CV (SS) indicate the corner vortices on the pressure and suction sides, respectively. The red dotted lines and dark blue arrows indicate clockwise rotation, whereas the yellow dotted lines and green arrows indicate counterclockwise rotation. Compared to the prototype cascade, the separation of the suction side was shifted back in Case 4, the starting position of the corner area was also shifted back, and the strength and range of the CV (SS) at the suction side were significantly reduced.

4. CONCLUSION

The flow control mechanism for the ellipsoidal dimples with different column numbers was numerically investigated for highly loaded compressor cascades, and the following conclusions were drawn:

(1) The ellipsoidal dimples improved the turbulent kinetic energy near the wall and redistributed the internal energy of the boundary layer, which led to an early transition of the boundary layer, thus delaying corner separation and changing or breaking the separation bubble. However, owing to the three-dimensional flow effect, the corner area at the trailing edge increased in the spanwise direction.

(2) Compared with the prototype cascade, the total pressure losses induced by the ellipsoidal dimples with 1–5 columns under the design conditions were reduced by 0.59%, 1.47%, 1.69%, 1.91%, and 1.73%, respectively.

(3) Through research on the formation and development of the vortex system in the flow passage, it was found that the elliptical concave cascade enhanced the momentum exchange between the low-energy fluid and the mainstream fluid in the boundary layer, improved the anti-separation ability of the fluid, and inhibited the migration of the transverse and spanwise secondary flows, thus weakening the ranges and intensities of the end-wall corner and passage vortices.

CONFLICT OF INTEREST

There is no conflict of interest to be declared in this work.

AUTHORS CONTRIBUTION

H. W. Lu: Conceptualization, Methodology, Project administration, Resources, Funding acquisition. **Y. P. Shi**: Methodology, Software, Validation, Formal analysis, Data curation, Visualization, Writing original draft preparation. **J. C. Xin**: Validation, Formal analysis, Data curation, Visualization. **X. Z. Kong**: Validation, Writing—review and editing, Supervision, Funding acquisition. **B. L. Peng**: Writing—review and editing.

REFERENCES

Amsha, K. A., Craft, T. J., & Iacovides, H. (2017). Computational modelling of the flow and heat transfer in dimpled channels. *The Aeronautical Journal, 121*(1242), 1066–1086. https://doi.org/10.1017/aer.2017.68

Cao, Z., Gao, X., Zhang, X., Zhang, F., & Liu, B. (2021). Influence of endwall air injection with discrete holes on corner separation of a compressor cascade. *Journal of Thermal Science*, *30*(5), 1684-1704. https://link.springer.com/article/10.1007/s11630-021-1513-5

Casey, J., King, P., & Sondergaard, R. (2004). *Parameterization of boundary layer control dimples on a low pressure turbine blade.* 40th AIAA/ASME/SAE/ASEE Joint Propulsion Conference and Exhibit. https://arc.aiaa.org/doi/abs/10.2514/6.2004-3570

Chen, H., Liu, H., Zhang, D., & Li, L. (2017, June). *Vortex structures for highly-loaded subsonic compressor cascades with slot injection.* Turbo Expo: Power for Land, Sea, and Air, American Society of Mechanical Engineers. https://doi.org/10.1115/GT2017-63781

Chen, Y., Yang, L., & Zhong, J. (2019). Numerical study on end wall fence with varying geometrical parameters in a highly-loaded compressor cascade. *Aerospace Science and Technology. 94*, 105390. https://doi.org/10.1016/j.ast.2019.105390

Chishty, M. A., Parvez, K., Ahmed, S., Hamdani, H. R., & Mushtaq, A. (2011, January). *Transition prediction in low pressure turbine (LPT) using gamma theta model and passive control of separation.* ASME International Mechanical Engineering Congress and Exposition. https://doi.org/10.1115/IMECE2011-62148

Chung, K. M., Su, K. C., & Chang, K. C. (2021). The Effect of vortex generators on shock-induced boundary layer separation in a transonic convex-corner flow. *Aerospace*. *8*, 157. https://doi.org/10.3390/aerospace8060157

D'Alessandro, V., Clementi, G., Giammichele, L., & Ricci, R. (2019). Assessment of the dimples as passive boundary layer control technique for laminar airfoils operating at wind turbine blades root region typical Reynolds numbers. *Energy*, *170*, 102-111. https://doi.org/10.1016/j.energy.2018.12.070

Jeong, H., & Song, S. J. (2021). Influence of surface roughness on the flat-plate boundary layer transition under a high-lift airfoil pressure gradient and low freestream turbulence. *American Society of Mechanical Engineers Digital Collection*, GT2021-59192. https://doi.org/10.1115/GT2021-59192

Lake, J., King, P., & Rivir, R. (1999). *Reduction of separation losses on a turbine blade with low Reynolds numbers.* 37th Aerospace Sciences Meeting and Exhibit. https://arc.aiaa.org/doi/abs/10.2514/6.1999-242

Lan, J., Xie, Y., & Zhang, D. (2011). Effect of leading edge boundary layer thickness on dimple flow structure and separation control. *Journal of Mechanical Science and Technology*, *25*, 3243-3251. https://doi.org/10.1007/s12206-011-0823-z

Liang, T., Liu, B., & Spence, S. (2021). Effect of boundary layer suction on the corner separation in a highly loaded axial compressor cascade. *American Society of Mechanical Engineers Digital Collection. 143*(6), 061002. https://doi.org/10.1115/GT2020-14566

Liesner, K., & Meyer, R. (2013). *Evaluation of passive and active secondary flow control in a high speed compressor cascade with different measurement techniques.* New Results in Numerical and Experimental Fluid Mechanics VIII: Contributions to the 17th STAB/DGLR Symposium Berlin, Germany 2010, Springer Berlin Heidelberg. https://doi.org/10.1007/978-3-642-35680-3_16

Lu, H. W., Yang, Y., Guo, S., Huang, Y. X., Wang, H., & Zhong, J. J. (2018a). The effect of dimpled surface on loss reduction and vortices in a highly loaded compressor cascade. *Proceedings of the Institution of Mechanical Engineers, Part G: Journal of Aerospace Engineering*, *232*(2), 374-387. https://doi.org/10.1177/0954410017728976

Lu, H. W., Yang, Y., Guo, S., Huang, Y. X., Wang, H., & Zhong, J. J. (2018b). Flow control in linear compressor cascades by inclusion of suction side dimples at varying locations. *Proceedings of the Institution of Mechanical Engineers, Part A: Journal of Power and Energy*, *232*(6), 706-721. https://doi.org/10.1177/0957650917752276

Lu, H., Yang, Y., Guo, S., Pang, W., Yang, F., & Zhong, J. (2019). Control of corner separation via dimpled surface for a highly loaded compressor cascade under different inlet Mach number. *Aerospace Science and Technology*, *85*, 48-60. https://doi.org/10.1016/j.ast.2018.11.054

Rao, Y., Li, B., & Feng, Y. (2015). Heat transfer of turbulent flow over surfaces with spherical dimples and teardrop dimples. *Experimental Thermal and Fluid Science*, *61*, 201-209. https://www.sciencedirect.com/science/article/abs/pii/S0894177714002829

Rouser, K. P. (2002). *Use of dimples to suppress boundary layer separation on a low pressure turbine blade* [Master's thesis, Department of Aeronautics and Astronautics]. https://scholar.afit.edu/etd/4139

Sondergaard, R., Rivir, R., Bons, J., & Yurchenko, N. (2004). *Control of separation in turbine boundary layers.* 2nd AIAA Flow Control Conference. https://doi.org/10.1016/j.energy.2018.12.070

Tian, L., Li, Z., Jin, E., Ke, Q., Dong, S., & Ma, Y. (2015). Improved flow performance of a centrifugal compressor based on pit formation on the notum of the whirligig beetle (Gyrinidae Latreille). *Advances in Mechanical Engineering*, *7*(7), 16878140-15591736. https://doi.org/10.1177/1687814015591736

Wang, L., Lu, H., Tian, Z., Yang, Y., Guo, S., Wang, H., & Kong, X. (2022). Numerical study of the ratio of

depth-to-print diameter on the performance and flow characteristics for a dimpled, highly loaded compressor cascade. *Aerospace*, *9*(8), 422. https://doi.org/10.3390/aerospace9080422

Wang. L., Lu, H., Guo, S., Pang, W., Song, H., & Yang, Y. (2020). Influence of arrangement of dimples on highly loaded compressor cascade. *Journal of Engineering Thermophilic, 41*(11), 2677-2686.

Xu, W., Sun, P., & Yang, G. (2021). Effect of the bionic chamber position on the aerodynamic performance in a transonic compressor cascade. *Aerospace Science and Technology*, *119*, 107106. https://doi.org/10.1016/j.ast.2021.107106

Zhang, H., Wu, Y., Li, Y., & Lu, H. (2015). Experimental investigation on a high subsonic compressor cascade flow. *Chinese Journal of Aeronautics*, *28*(4), 1034-1043. https://doi.org/10.1016/j.cja.2015.06.019

Zhang, H., Yu, X., Liu, B., Wu, Y., & Li, Y. (2017). Control of corner separation with plasma actuation in a high-speed compressor cascade. *Applied Sciences*, *7*(5), 465. https://doi.org/10.3390/app7050465

Zhao, Y., Lu, H., & Sun, Y. (2016). Experimental studies of dimpled surface effect on the performance of linear cascade under different incidence angles. *Procedia CIRP*, *56*, 137-142. https://doi.org/10.1016/j.procir.2016.10.043

Zinchenko, I. M., Skoryk, A., & Parafejnik, V. (2016). On the effect of spherical dimples at diffuser vane surface on performance of centrifugal compressor. *NTU "KhPI" Bulletin: Power and Heat Engineering Processes and Equipment*, (9), 37-43. https://doi.org/10.20998/2078774X.2016.09.05